



Magnetic Helicity Reversal in the Corona at Small Plasma Beta

Philippe Bourdin¹ , Nishant K. Singh^{2,3} , and Axel Brandenburg^{3,4,5,6} ¹ Space Research Institute, Austrian Academy of Sciences, Schmiedlstr. 6, A-8042 Graz, Austria; Philippe.Bourdin@oeaw.ac.at² Max-Planck-Institut für Sonnensystemforschung, Justus-von-Liebig-Weg 3, D-37077 Göttingen, Germany³ Nordita, KTH Royal Institute of Technology and Stockholm University, Roslagstullsbacken 23, SE-10691 Stockholm, Sweden⁴ JILA and Department of Astrophysical and Planetary Sciences, University of Colorado, Boulder, CO 80303, USA⁵ Department of Astronomy, AlbaNova University Center, Stockholm University, SE-10691 Stockholm, Sweden⁶ Laboratory for Atmospheric and Space Physics, University of Colorado, Boulder, CO 80303, USA

Received 2018 April 11; revised 2018 October 17; accepted 2018 October 17; published 2018 December 5

Abstract

Solar and stellar dynamos shed small-scale and large-scale magnetic helicity of opposite signs. However, solar wind observations and simulations have shown that some distance above the dynamo both the small-scale and large-scale magnetic helicities have reversed signs. With realistic simulations of the solar corona above an active region now being available, we have access to the magnetic field and current density along coronal loops. We show that a sign reversal in the horizontal averages of the magnetic helicity occurs when the local maximum of the plasma beta drops below unity and the field becomes nearly fully force free. Hence, this reversal is expected to occur well within the solar corona and would not directly be accessible to in situ measurements with the *Parker Solar Probe* or *Solar Orbiter*. We also show that the reversal is associated with subtle changes in the relative dominance of structures with positive and negative magnetic helicity.

Key words: dynamo – magnetohydrodynamics (MHD) – methods: numerical – Sun: corona – Sun: magnetic fields – solar wind

1. Introduction

Magnetic helicity is an important invariant in ideal and nearly ideal magnetohydrodynamics (MHD); see Biskamp (2003) and the original work of Woltjer (1958). It plays a crucial role in characterizing the topological complexity of coronal magnetic fields (Berger & Field 1984), and it is also responsible for the possibility of premature quenching of the underlying dynamo (Gruzinov & Diamond 1994). An obvious remedy to the dynamo problem is to let excess magnetic helicity escape through the boundaries (Blackman & Field 2000; Kleeorin et al. 2000), especially through coronal mass ejections (Blackman & Brandenburg 2003) and the solar differential rotation, which also acts on open field lines rooted in magnetically quiet regions of the photosphere (DeVore 2000); see Berger & Ruzmaikin (2000) for estimates of the relative importance of different contributions to the total magnetic helicity flux. Much of the magnetic helicity transported by differential rotation out through the surface has entered through the equator; see Brandenburg & Sandin (2004). Its contribution to the net magnetic helicity loss may therefore be subdominant. Nevertheless, estimates for the Sun invariably result in a total loss of $\mp 10^{46}$ Mx² per 11 year cycle (Berger & Ruzmaikin 2000; DeVore 2000; Brandenburg & Sandin 2004; Brandenburg 2009) in the northern and southern hemispheres, respectively. One would therefore expect to see that the magnetic helicity shed at the solar surface agrees with what is passing through the solar wind at larger distances. However, this does not seem to be the case because in the solar wind, the magnetic helicity was found to have mostly a positive sign in the northern heliosphere (Brandenburg et al. 2011), whereas at the solar surface it is mostly negative in the north (Seehafer 1990). A similar result was also obtained in numerical simulations of dynamos with a coronal exterior (Warnecke et al. 2011, 2012). This unexpected behavior is what is referred to as magnetic helicity reversal. Such reversals

have also been found in analytic solutions of simple dynamo models with a force-free exterior (Bonanno 2016) and in mean-field models with magnetic helicity fluxes included (Brandenburg et al. 2009).

Numerical simulations are currently the best way of testing and studying in detail the idea of the magnetic helicity reversal. Here, we consider the magnetic helicity that was found to emerge from the MHD simulations of Bourdin et al. (2013, hereafter **BBP**), who used a solar magnetogram of an active region (AR) as a boundary condition. Reconnection and the associated coronal heating were driven by random footpoint motions, as envisaged in the early work of Parker (1972). The simulations of **BBP** used the PENCIL CODE⁷ and covered a larger domain ($235^2 \times 156$ Mm³) compared to earlier ones with the STAGGER CODE (Gudiksen & Nordlund 2002, 2005a, 2005b).

The AR model of **BBP** is observationally driven by line-of-sight magnetograms taken from HINODE/SOT-NFI (Kosugi et al. 2007; Tsuneta et al. 2008). The model provides a sufficient amount of energy to the corona (Bourdin et al. 2015). It also compares well with various coronal observations (**BBP**) and shows similarities to coronal scaling laws, e.g., for the temperature along loops that were derived from earlier observational and theoretical works (cf. Bourdin et al. 2016).

The coronal EUV emission is synthesized from the MHD model using the CHIANTI atomic database (Dere et al. 1997; Young et al. 2003) using the method of Peter et al. (2004, 2006). The 3D structure of the AR loop system matches the reconstruction from STEREO observations. Also, the plasma flow dynamics along those loops matches the Doppler shift pattern observed by HINODE/EIS (Culhane et al. 2007) in the coronal Fe XII emission line.

The magnetograms for driving these simulations from the bottom boundary give just the line-of-sight magnetic field, or

⁷ <https://github.com/pencil-code>

B_z near disk center. During the first hour of solar time, we do not yet apply any large-scale driving motions derived from the observed movements of magnetic patches in the photosphere. We only apply the horizontal small-scale velocities that mimic granulation. Therefore, these photospheric horizontal motions are purely stochastic and statistically mirrorsymmetric, and there is no obvious mechanism to break the statistical mirrorsymmetry of the model. In particular, there is no Coriolis force or differential rotation. Nonetheless, it turns out that helicity emerges readily within the initial phase of our model.

Although there is no direct injection of helicity, the model can still produce magnetic helicity through a complex arrangement of multipolar spots (Bourdin & Brandenburg 2018). We use a magnetogram of a small and stable AR observed during 2007 November 14 in the southern hemisphere. Indeed, we find helicity, as is readily demonstrated by looking at the vertical profile of the mean current helicity density, $\langle \mathbf{J} \cdot \mathbf{B} \rangle_{xy}$, where $\mathbf{J} = \nabla \times \mathbf{B} / \mu_0$ is the current density, \mathbf{B} is the magnetic field, μ_0 is the vacuum permeability, and $\langle \dots \rangle_{xy}$ denotes horizontal averages. We find that the profiles generally show a sign reversal within the first 5–15 Mm above the surface. This is equally remarkable because the upper regions are topologically connected with the lower ones through the same large-scale structures. Any small-scale magnetic fields seem to be interspersed within other structures and are still associated with the large-scale magnetic loops extending from one footpoint to the other.

The purpose of this work is to quantify the magnetic helicity reversal in detail and to associate it with coronal heating along EUV-emissive loops. We further characterize the magnetic helicity reversal in spectral space and demonstrate that it occurs in different wavenumber intervals at the same height.

2. Our Approach

In the present work, we use a snapshot from the simulations of [BBP](#) to analyze the production and vertical variation of magnetic and current helicity densities as well as their spectra. Before discussing those aspects in detail, we begin with the basic equations solved in [BBP](#) and present a brief summary of the physical properties of those simulations.

2.1. Basic Equations

[BBP](#) solved the continuity equation, the equation of motion, the induction equation, and an energy equation, which includes the necessary energy sinks to get realistic and self-consistent coronal heating and cooling terms:

$$\frac{D \ln \rho}{Dt} = -\nabla \cdot \mathbf{u}, \quad (1)$$

$$\rho \frac{D\mathbf{u}}{Dt} = -\nabla P + \rho \mathbf{g} + \mathbf{J} \times \mathbf{B} + \nabla \cdot (2\nu \rho \mathbf{S}), \quad (2)$$

$$\rho T \frac{Ds}{Dt} = -\nabla \cdot \mathbf{F} - \rho^2 \Lambda(T) + \mu_0 \eta \mathbf{J}^2 + 2\rho \nu \mathbf{S}^2, \quad (3)$$

$$\frac{\partial \mathbf{A}}{\partial t} = \mathbf{u} \times \mathbf{B} - \mu_0 \eta \mathbf{J}, \quad (4)$$

where $P = (\mathcal{R}/\mu) \rho T$ is the gas pressure, \mathcal{R} is the universal gas constant, $\mu = 0.67$ is the mean atomic mass, T is the temperature, $F_i = -\rho c_p \chi_{ij} \nabla_j T$ is the conductive heat flux, $s = c_v \ln P - c_p \ln \rho + s_0$ is the specific entropy, s_0 is a constant, c_p and c_v are the specific heats at constant pressure

and constant volume, respectively, $\chi_{ij} = \chi_0 \delta_{ij} + \chi_{\text{Spitz}} \hat{B}_i \hat{B}_j$ is the thermal diffusivity, $\hat{\mathbf{B}}$ is the unit vector of the magnetic field, ν is the kinematic viscosity, η is the magnetic diffusivity, χ_{Spitz} is the Spitzer field-aligned heat conductivity, χ_0 is an isotropic contribution, \mathbf{g} is the gravitational acceleration, and \mathbf{S} is the traceless rate-of-strain tensor with the components $S_{ij} = \frac{1}{2}(u_{i,j} + u_{j,i}) - \frac{1}{3}\delta_{ij}u_{k,k}$. Here, we solve for \mathbf{A} because then \mathbf{B} is automatically divergence free. Instead of solving for s , we use the logarithmic temperature $\ln T$, which is directly related to s and $\ln \rho$. Using the logarithmic density $\ln \rho$, we are able to capture many orders of magnitude in the density stratification that our model atmosphere covers.

2.2. Physical Details about the Simulations

For the radiative cooling function $\rho \Lambda(T)$, we use a realistic tabulation of Λ provided by Cook et al. (1989). In that work, the important emission peak from highly ionized iron lines is included, which efficiently cools the model corona. The characteristic half-time of this cooling is below 30 minutes.

During the first 35 minutes of physical time, however, this loss term is turned off together with the heat conduction along the field. This is to prevent excessive cooling of the corona during the initial phase in which the granular motions cause magnetic disturbances that still need to propagate from the photosphere into the corona. The simulation is then continued for another about 35 minutes after all physical terms in the equations are turned on. Further details about the switching on can be found in Bourdin et al. (2014) and Bourdin (2014). We use here data from a fully developed state at 63 minutes physical time.

Unlike ideal models of MHD, where $\eta = \nu = 0$ and dissipation is modeled by highly nonlinear diffusion operators that cannot easily be stated in concise form and effective Reynolds or Lundquist numbers are difficult to specify, we use in our model constant values of ν , η , and also χ_0 . The value of the magnetic diffusivity $\eta = 10^{10} \text{ m}^2 \text{ s}^{-1}$ ($=10^{14} \text{ cm}^2 \text{ s}^{-1}$) is about eight orders of magnitude bigger than that estimated for the solar corona. This choice is required for numerical stability and for having a grid Reynolds number near unity. On the other hand, we use a realistic value for the viscosity, $\nu = 10^{10} \text{ m}^2 \text{ s}^{-1}$, which results in a Prandtl number of unity because $\eta = \nu$. However, as pointed out by Rempel (2017), the relative importance of Ohmic and viscous heating changes toward the latter when realistically large values of the magnetic Prandtl numbers are taken into account; see Brandenburg (2014) for the relation between the dissipation ratio and the magnetic Prandtl number. The isotropic heat conduction is set to $\chi_0 = 5 \times 10^8 \text{ m}^2 \text{ s}^{-1}$ ($=5 \times 10^{12} \text{ cm}^2 \text{ s}^{-1}$). We use a realistic coronal value of $\kappa_{\text{Spitz}} = 1.8 \cdot 10^{-10} T^{5/2} / \ln \Lambda_C$ with $\ln \Lambda_C = 20$ being the Coulomb logarithm. We obtain the field-aligned Spitzer conductivity as

$$\chi_{\text{Spitz}} = \frac{1}{c_p} \kappa_{\text{Spitz}} T^{5/2} / \rho. \quad (5)$$

2.3. Boundary Conditions

The model is periodic in the horizontal directions and employs a potential-field extrapolation on the top boundary. To formulate the potential-field boundary condition, we define the

Fourier-transformed magnetic vector potential as

$$\tilde{\mathbf{A}}(k_x, k_y, z, t) = \int \mathbf{A}(x, y, z, t) e^{i\mathbf{k}\cdot\mathbf{r}} d^2\mathbf{r}, \quad (6)$$

where $\mathbf{k} = (k_x, k_y)$ and $\mathbf{r} = (x, y)$. On the lower and upper z boundaries, we thus have

$$\frac{\partial \tilde{\mathbf{A}}}{\partial z} = -|\mathbf{k}| \tilde{\mathbf{A}}(k_x, k_y, z_*, t), \quad (7)$$

where z_* denotes the locations of the boundaries. Apart from this, the top boundary is closed for any plasma flows and is thermally insulating.

At the bottom boundary, realistic atmospheric temperature and density are imposed. We also adopt Equation (7) at the bottom boundary, but keep the minus sign on the right-hand side. This corresponds to an inverted potential-field extrapolation, whereby contrasts in the magnetic field are increased, instead of smearing them out like for the top boundary. This mimics the effect of flux tubes becoming narrower when entering below the photosphere. Because this increase of contrast would quickly lead to artifacts, like wiggles in the B_z component, this increase of contrast is limited to about one-third of the pressure scale height some 100 km below the photosphere so that artifacts in B_z are avoided. With this method, we obtain the ghost zones for all three components of \mathbf{A} just beneath the lower photospheric boundary.

2.4. Gauge Dependence of Magnetic Helicity

In general, the local magnetic helicity density

$$\mathcal{H}_M = \mathbf{A} \cdot \mathbf{B} \quad (8)$$

depends on the gauge of the vector potential \mathbf{A} . On the lower and upper boundaries of the simulation domain, our magnetic field is driven toward a potential state. The resulting \mathbf{A} at these boundaries is in the Weyl gauge. However, the gauge could in principle still drift because we have no boundary restrictions other than periodicity along x and y . Therefore, we must check if such a gauge drift occurs and if it significantly changes our simulation results.

We use the relative helicity from Equation (5) of Finn & Antonsen (1985), similar to the formulation of Berger & Field (1984), to obtain a gauge-independent helicity as

$$\mathcal{H}_{M,\text{rel}}(z) = \iiint_z^\infty \frac{1}{2} (\mathbf{A} + \mathbf{A}_{\text{pot}}) \cdot (\mathbf{B} - \mathbf{B}_{\text{pot}}) dz dy dx. \quad (9)$$

\mathbf{A}_{pot} and \mathbf{B}_{pot} are the nonhelical potential fields extrapolated from the known state of $B_z(z)$ at the height z . On the upper boundary $z = L_z$, our magnetic field is already almost potential and very close to the nonhelical extrapolation $\mathbf{B}_{\text{pot}}(L_z)$. The magnetic helicity therefore vanishes toward the top of the domain and we may omit the volume from L_z to ∞ in the integrals of H_{rel} . Our factor of one-half compensates for the addition of the two similar quantities \mathbf{A} and \mathbf{A}_{pot} in Equation (9), which allows the relative magnetic helicity to be quantitatively similar to the magnetic helicity \mathcal{H}_M . Because the components of \mathbf{B} and \mathbf{B}_{pot} are normal to all nonperiodic boundaries (here, the top and bottom of the simulation domain), they are either identical by construction or their differences are negligible. Equation (9) gives us therefore a

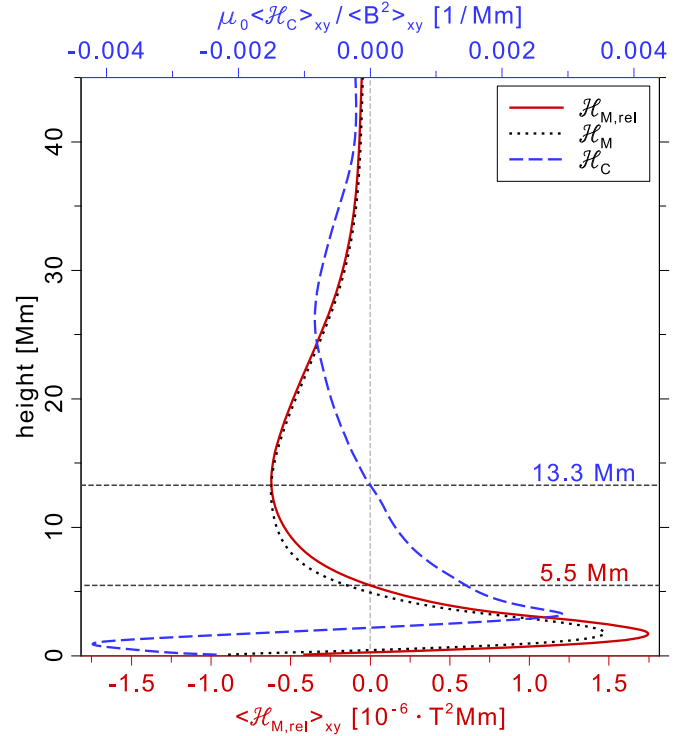


Figure 1. Horizontal averages of the gauge-dependent magnetic helicity, the gauge-independent relative helicity, and the current helicity normalized to B^2 vs. height.

gauge-independent relative helicity (Berger & Field 1984; Finn & Antonsen 1985).

To compare a vertical profile of \mathcal{H}_M and $\mathcal{H}_{M,\text{rel}}$, we compute the horizontal averages of both quantities. To get $\langle \mathcal{H}_M(z) \rangle_{xy}$ of the magnetic helicity density $\mathcal{H}_M(z)$, we simply average over horizontal slices from the height z and with a thickness of Δz equal to our vertical grid spacing. For the profile of $\mathcal{H}_{M,\text{rel}}(z)$, we simply subtract the volume integrals above the heights z and $z + \Delta z$. Each integral uses different potential fields, $\mathbf{A}, B_{\text{pot},z}$ and $\mathbf{A}, B_{\text{pot},z+\Delta z}$, which we extrapolate from the known states $B_z(z)$ and $B_z(z + \Delta z)$, respectively. The average relative magnetic helicity density contained in this xy layer is then just the difference

$$\langle \mathcal{H}_{M,\text{rel}} \rangle_{xy}(z) = \frac{\mathcal{H}_{M,\text{rel}}(z) - \mathcal{H}_{M,\text{rel}}(z + \Delta z)}{V_{xy\Delta z}}, \quad (10)$$

which we normalize to the volume of the layer $V_{xy\Delta z}$ to be comparable to $\langle \mathcal{H}_M(z) \rangle_{xy}$; see Figure 1.

We find that the horizontal averages of our magnetic helicity density \mathcal{H}_M and the relative helicity density $\mathcal{H}_{M,\text{rel}}$ are very similar. Both magnetic helicities do show sign reversals that are located roughly at the same height, like the maxima and minima; see the dotted and red lines in Figure 1. The vertical profile of the current helicity, $\mathcal{H}_C = \mu_0 \mathbf{j} \cdot \mathbf{B}$, shows a qualitatively similar trend also with a sign reversal in the corona, albeit higher up; see the blue dashed line. We show that our magnetic helicity density is therefore not significantly influenced by the gauge drift along the periodic directions. Therefore, we may continue to use the gauge-dependent magnetic helicity \mathcal{H}_M as a good proxy of the gauge-independent relative helicity $\mathcal{H}_{M,\text{rel}}$.

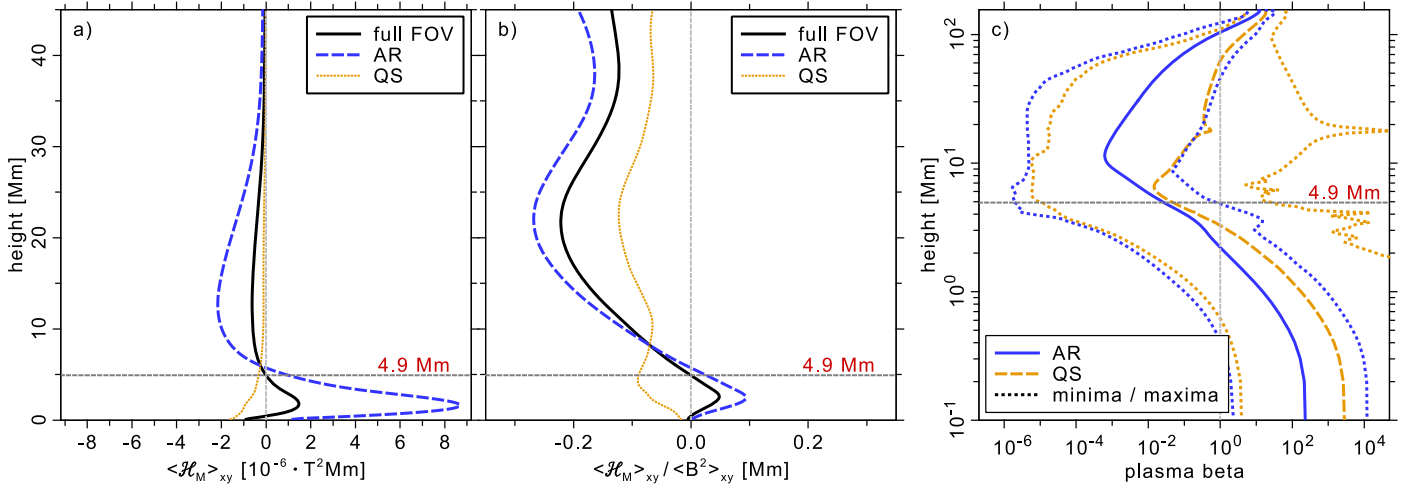


Figure 2. (a) Magnetic helicity for the full FOV, the AR core, and only the QS area as a profile of horizontal averages vs. height. (b) Magnetic helicity normalized to B^2 . (c) Plasma beta value ranges for AR and QS.

2.5. Magnetic and Current Helicity Spectra

Through most of this work, we show both current and magnetic helicity. In particular, we consider two-dimensional current and magnetic helicity spectra defined as

$$H_C(k) = \frac{1}{2} \sum_{k_- < |\mathbf{k}| \leq k_+} (\tilde{\mathbf{J}} \cdot \tilde{\mathbf{B}}^* + \tilde{\mathbf{J}}^* \cdot \tilde{\mathbf{B}}), \quad (11)$$

$$H_M(k) = \frac{1}{2} \sum_{k_- < |\mathbf{k}| \leq k_+} (\tilde{\mathbf{A}} \cdot \tilde{\mathbf{B}}^* + \tilde{\mathbf{A}}^* \cdot \tilde{\mathbf{B}}), \quad (12)$$

where $k_{\pm} = k \pm \delta k/2$ and $\delta k = 2\pi/L$ with $L = 235$ Mm being the size of the magnetograms and tildes denote, again, Fourier transformation. Under horizontally isotropic conditions, we have

$$\mu_0 H_C(k) = k^2 H_M(k), \quad (13)$$

i.e., the current helicity spectrum is directly related to the magnetic helicity spectrum, but weighted with a k^2 factor, so high wavenumber contributions in $H_M(k)$ get enhanced.

It is sometimes convenient to define the magnetic and current helicity densities as

$$\mathcal{H}_M = \mathbf{A} \cdot \mathbf{B}, \quad \mathcal{H}_C = \mathbf{J} \cdot \mathbf{B}. \quad (14)$$

Note, in particular, that at each value of z , we have

$$\int H_M dk = \langle \mathcal{H}_M \rangle_{xy}, \quad \int H_C dk = \langle \mathcal{H}_C \rangle_{xy}. \quad (15)$$

In the following, however, we often retain the more explicit notation in terms of $\mathbf{A} \cdot \mathbf{B}$ and $\mathbf{J} \cdot \mathbf{B}$.

3. Results

3.1. Magnetic Helicity Reversal

To set the stage, we show in Figure 2 vertical profiles of $\langle H_M \rangle_{xy}$, $\langle H_M \rangle_{xy} / \langle B^2 \rangle_{xy}$, and the plasma beta, $2\mu_0 \langle P \rangle_{xy} / \langle B^2 \rangle_{xy}$ (cf. Bourdin 2017). For comparison, we also plot the corresponding profiles for averages over the AR core and the complementary quiet-Sun (QS) area. For the plasma beta, we also show minimum and maximum values (dotted). In the lower part, for $z \lesssim 5$ Mm, $\langle \mathbf{A} \cdot \mathbf{B} \rangle_{xy}$ is positive, while for $z \gtrsim 5$ Mm it is negative. In fact, for the full field of view (FOV), and in a small z interval very close to the lower

boundary, the sign of $\langle \mathbf{A} \cdot \mathbf{B} \rangle_{xy}$ changes once again. We return to this aspect again later.

The main focus of this paper is instead the sign reversal of $\langle \mathbf{A} \cdot \mathbf{B} \rangle_{xy}$ at $z \approx 5$ Mm. This happens at a height where the magnetic field begins to become almost force free; see Figure 2(a). To assess this quantitatively, we plot in Figure 3 vertical profiles of the characteristic nondimensional wavenumbers $\kappa_{\mathbf{J} \cdot \mathbf{B}}$ and $\kappa_{\mathbf{J} \times \mathbf{B}}$ defined through (Warnecke & Brandenburg 2010)

$$\kappa_{\mathbf{J} \cdot \mathbf{B}}^2 \equiv \frac{\langle (\mathbf{J} \cdot \mathbf{B})^2 \rangle_{xy}}{\langle \mathbf{J}^2 \mathbf{B}^2 \rangle_{xy}}, \quad \kappa_{\mathbf{J} \times \mathbf{B}}^2 \equiv \frac{\langle (\mathbf{J} \times \mathbf{B})^2 \rangle_{xy}}{\langle \mathbf{J}^2 \mathbf{B}^2 \rangle_{xy}}. \quad (16)$$

Note that $\kappa_{\mathbf{J} \cdot \mathbf{B}}^2 + \kappa_{\mathbf{J} \times \mathbf{B}}^2 = 1$, so the two are complementary in the sense that when $\kappa_{\mathbf{J} \times \mathbf{B}} \rightarrow 0$, we have $\kappa_{\mathbf{J} \cdot \mathbf{B}} \rightarrow 1$, and vice versa. Looking at Figure 3, we see that in $5 \text{ Mm} \lesssim z \lesssim 50 \text{ Mm}$, the magnetic field is indeed nearly force free and $\kappa_{\mathbf{J} \cdot \mathbf{B}}$ reaches values close to unity, the largest possible value. Consequently, $\kappa_{\mathbf{J} \times \mathbf{B}}$ is very small in this range for AR and QS.

3.2. Magnetic Helicity Reversal within a Flux Rope

In Figure 4, we show a visualization of $\mathbf{A} \cdot \mathbf{B}$. We see that the magnetic helicity density changes in a horizontal plane at approximately 5 Mm. We also show the magnetic helicity density in several yz planes through two particularly prominent magnetic field lines labeled as CL1 and CL2, where CL1 is a EUV-emissive loop in the core of the AR. While one of the two field lines passes through regions where $\mathbf{A} \cdot \mathbf{B}$ is positive (red) throughout, the other field line traverses yz planes in which $\mathbf{A} \cdot \mathbf{B}$ is positive near the apex of the line (denoted by CL2) and negative in the xy plane through 5 Mm (denoted by CL1). This shows that at least one magnetic helicity reversal is possible right in the middle of a field line or loop.

The loops SL1–3 connect from one of the main polarities to the periphery of the AR. SL1–3 show strongly asymmetric heating and EUV emissivity. We find that the coronal heating is particularly strong on that side, where SL1–3 are rooted in strong negative magnetic helicity (blue in Figure 4). The other end of these side loops connects to low-helicity areas and there we also see less heating and EUV emissivity. Note that under the assumption of horizontal isotropy leading to Equation (13),

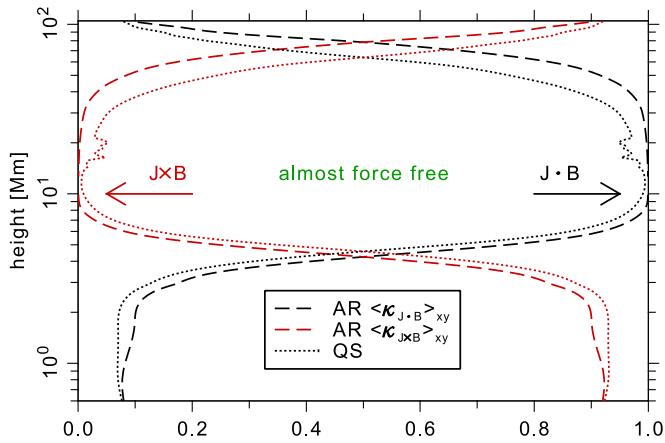


Figure 3. Force-free parameters $\kappa_{J \cdot B}$ and $\kappa_{J \times B}$ for the AR core area and the complementary QS area. At $z = 10$ Mm, the magnetic field is nearly fully force free, so $\kappa_{J \times B} \rightarrow 0$ and $\kappa_{J \cdot B} \rightarrow 1$.

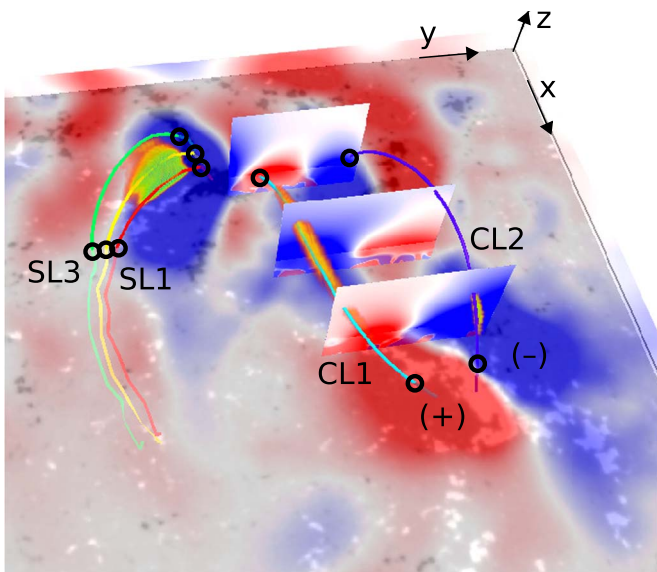


Figure 4. Visualization of coronal loops (field lines) with EUV emission (orange–green volume rendering) above an AR magnetogram (grayscale at the bottom). The semi-transparent layer at 5.5 Mm shows the magnetic helicity density with positive to negative values color-coded from red to blue, saturated at $\pm 0.2 \times 10^{-3} \text{ T}^2 \text{ Mm}$. The black circles mark where the field lines cross this horizontal layer. Three vertical opaque planes cut through the cross section of the loops in the core of the AR and also indicate the magnetic helicity density, but saturated at $\pm 0.1 \times 10^{-3} \text{ T}^2 \text{ Mm}$; see Section 3.2.

both the current helicity and magnetic helicity spectra are related. In particular, since the spectral magnetic helicity reflects the large-scale properties of current helicity, it corresponds to the integral over all large-scale patches of the current helicity density.

We also note that the most strongly heated core-loop CL1 is rooted in two strong positive helicity regions (red in Figure 4), and at the same time, we find a negative helicity (blue) near the loop apex. While we do not want to claim a direct relation of magnetic helicity and the coronal Ohmic dissipation of currents that heats our model loops, we need to point out that local injection of helicity is a way of transporting magnetic energy to the corona and induce currents there. Nonetheless, this could only demonstrate that the volumetric heating and the EUV emissivity is of course strongly modulated by density variations. In particular, when the density is low, the heating

per particle is high. Therefore, one would not see a clear one-to-one correlation of helicity and the coronal heating or EUV emission.

3.3. Spectral Magnetic Helicity Reversal

The study of magnetic helicity spectra has revealed important insights about the nature of the turbulent dynamo; see Brandenburg & Subramanian (2005) for a review. Owing to magnetic helicity conservation, the α effect in mean-field electrodynamics (Moffatt 1978; Krause & Rädler 1980) can only produce positive and negative magnetic helicities to equal amounts, but at different length scales (Seehafer 1996; Ji 1999). This leads to a bihelical magnetic field (Blackman & Brandenburg 2003; Yousef & Brandenburg 2003) with one sign at the scale of the energy carrying eddies (referred to as “small scale”) and another sign at the scale of the domain (referred to as “large scale”). In the solar wind, the spectrum is also found to be bihelical, but the signs at both small and large scales are reversed (Brandenburg et al. 2011). In the MHD model, the photospheric structures are “small scale” and smear out when reaching higher atmospheric layers. Coronal loops then define the “large scale” structures. The basic question is now whether this apparent swap in sign at small and large scales happens abruptly at one particular height and across all scales, or gradually through an effective shift of the spectrum in wavenumber, as perhaps suggested by the idea of an inverse cascade behavior, where the height in the domain plays the role of time in a decaying MHD simulation; see Christensson et al. (2001) for an example in the cosmological context.

The result is shown in Figure 5 where we compare visualizations of both $\mathbf{A} \cdot \mathbf{B}$ and $\mathbf{J} \cdot \mathbf{B}$ in six horizontal planes with the corresponding spectra $k^2 H_M(k)$ and $H_C(k)$ obtained in the same six planes. Note first of all that the two spectra look similar in shape and magnitude at corresponding heights, suggesting that the relation between them, as given in Equation (13) for isotropic turbulence, is reasonably well obeyed. The spectra vary over more than 10 orders of magnitude, falling steeply with wavenumber, with its largest values corresponding to the smallest few wavenumbers that dominate the overall sign of the total integrated magnetic and current helicities. In the first three slices up to $z \approx 5$ Mm, the dominant signs of $k^2 H_M(k)$ and $H_C(k)$ are negative for $k > 3 \text{ Mm}^{-1}$ and positive for $k < 3 \text{ Mm}^{-1}$. Above this layer, the sign of $k^2 H_M(k)$ reverses abruptly in the sense that it is now negative (positive) for k smaller (larger) than 3 Mm^{-1} . However, the sign of $H_C(k)$ varies more gradually with height, showing a similar reversal only at $z \approx 13$ Mm; see also Figure 7. Interestingly enough, at a fixed height, both below and above the transition layer at $z \approx 5$ Mm where the sign reversal of the magnetic helicity occurs, the spectrum $k^2 H_M(k)$ changes its sign in k space at roughly the same value of k , namely at $k \approx 3 \text{ Mm}^{-1}$. This supports the notion that this phenomenon is related to a change in the relative dominance of structures of opposite sign of $\mathbf{J} \cdot \mathbf{B}$, as discussed above in Section 3.2, and is not due to a shift in k , which would be more reminiscent of an inverse cascade-type behavior.

We reiterate that $H_M(k)$ is gauge independent. It is therefore important to emphasize that the magnetic and current helicity reversals are also seen in specific wavenumber intervals (e.g., for k larger or smaller than 3 Mm^{-1}). Moreover, the reversals occur at the same height as those in $\mathbf{A} \cdot \mathbf{B}$. This supports the notion that the sign change in $\mathbf{A} \cdot \mathbf{B}$ is not compromised by its

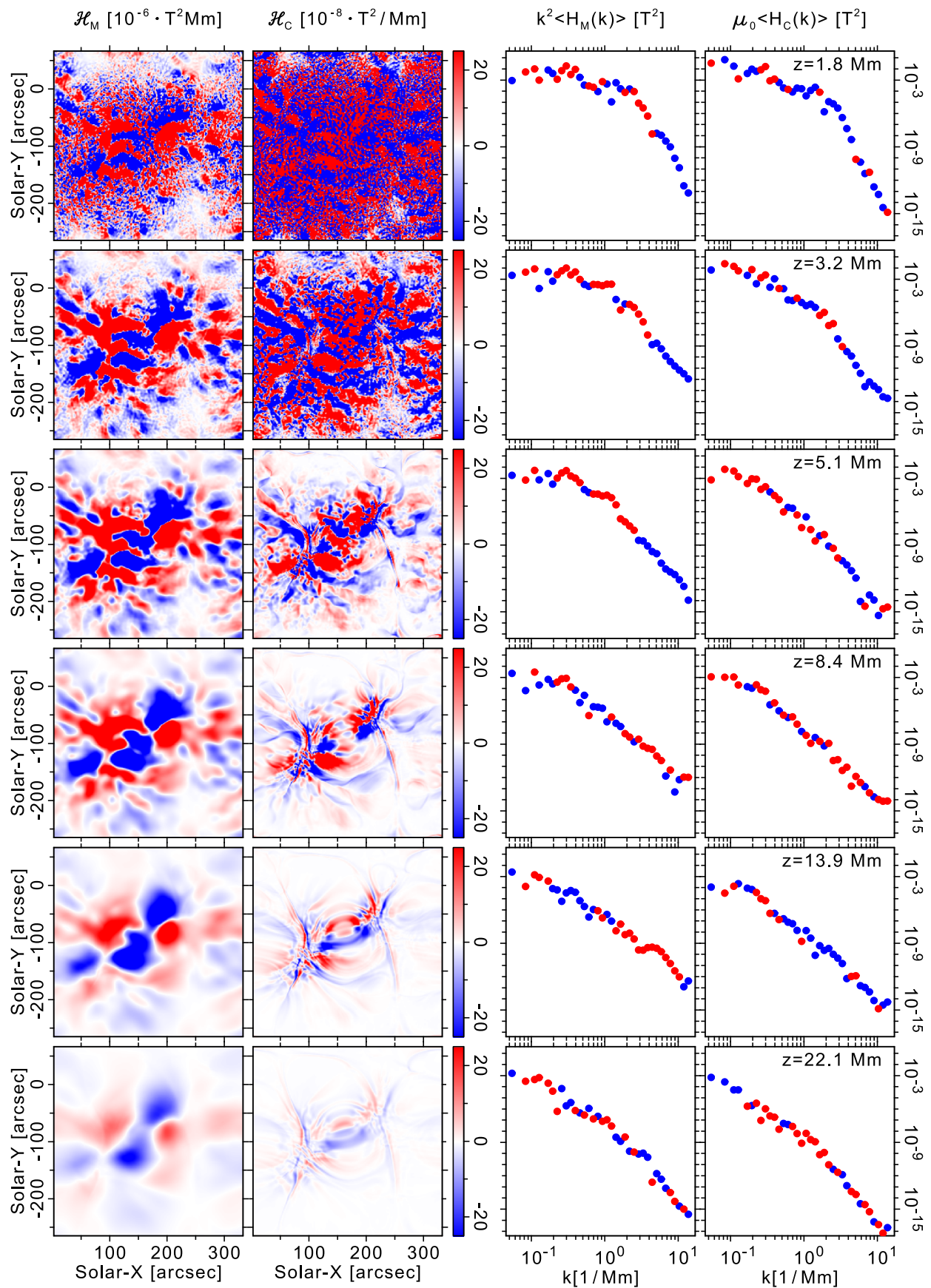


Figure 5. Horizontal maps of the magnetic helicity (column 1; leftmost) and current helicity (column 2) densities for six different heights. Spectra of the magnetic helicity (column 3) and current helicity (column 4) densities. Positive (negative) values are shown in red (blue).

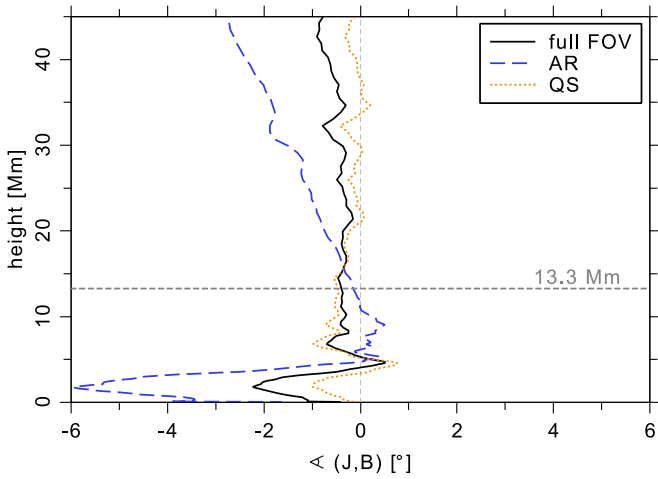


Figure 6. Average angle between \mathbf{J} and \mathbf{B} .

gauge dependence; see also Figure 1 and Section 2.4. Furthermore, the upper boundary condition Equation (7) always tends to relax \mathbf{A} back to zero, as any contrasts get smeared out by the potential-field extrapolation. The A_x and A_y components are set through the lower boundary condition to match the observed B_z component. Hence, any drift in \mathbf{A} will be suppressed.

3.4. Nearly Perfectly Field-aligned Currents

Within the lower corona, in the range $5 \text{ Mm} \lesssim z \lesssim 50 \text{ Mm}$, the plasma beta is around 10^{-2} or less; see Figure 2(c). The magnetic field here is nearly fully force free; see Figure 3. In this range, the angle

$$\langle (\mathbf{J}, \mathbf{B}) \rangle = \arccos(\mathbf{J} \cdot \mathbf{B} / (|\mathbf{J}| |\mathbf{B}|)) \quad (17)$$

between \mathbf{J} and \mathbf{B} is on average very small. Closer to the surface, for $z < 5 \text{ Mm}$, larger values can be found, but even then the angles are hardly much larger than $\pm 2^\circ$; see Figure 6. Only above the AR can larger angles of up to $\pm 8^\circ$ be found.

3.5. An Additional Current Helicity Reversal

Very near the surface, we have seen in Figure 2 for the full FOV an additional reversal in magnetic helicity very close to the surface. Looking at a similar plot of current helicity, we see that this secondary reversal is now more pronounced and includes even the AR. In current helicity, the secondary reversal is seen at $z \approx 2 \text{ Mm}$. Furthermore, the primary reversal occurs higher up at about 13 Mm. The reason for this secondary reversal becomes more plausible when looking at the horizontal distribution of $\mathbf{J} \cdot \mathbf{B}$ in Figure 7, which shows that there are *always* nearly equally many and nearly equally large patches of both helicities. Thus, the dominance of one sign over the other depends on small changes in the relative strengths of structures with positive and negative contributions to $\mathbf{J} \cdot \mathbf{B}$. The second reversal in current helicity is obviously a real phenomenon in the present simulations, but it is unclear whether it is also a generic phenomenon of stratified and magnetized atmospheres in general. Furthermore, in magnetic helicity, it was only seen in the full FOV and not above the AR. Comparing the maps of magnetic and current helicities shown in Figure 5, we see that \mathcal{H}_C is more noisy, and therefore the additional reversal does not appear to be a systematic feature. More important to note is that the magnetic helicity associated

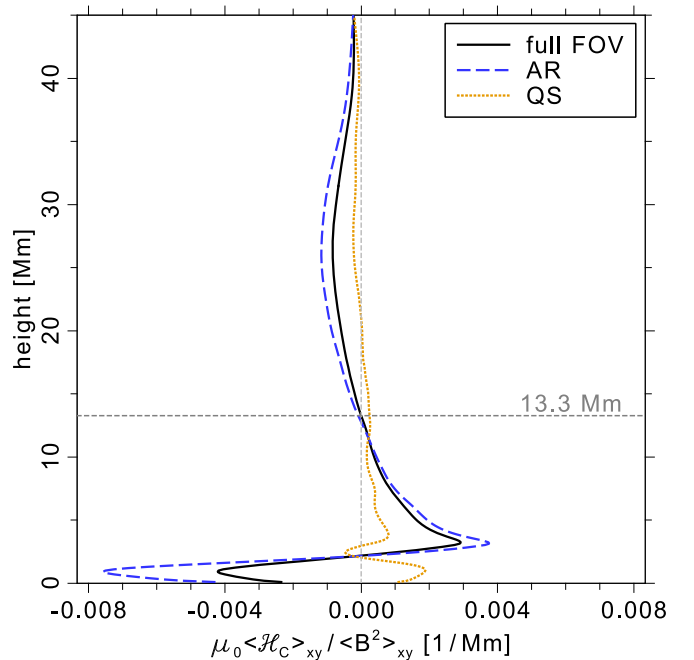


Figure 7. Current helicity for AR and QS vs. height.

with the AR is positive near the surface, exactly as would be expected for the southern hemisphere based on an α effect-driven turbulent dynamo.

Looking once more at Figure 5, it becomes clear that the negative sign of magnetic helicity in the uppermost layers can be associated with a single structure that persists in all the horizontal maps of $\mathbf{A} \cdot \mathbf{B}$ between 3 and 22 Mm. This persistent helicity patch is located in the AR core near the legs of the loop CL1 that are indicated by black circles in Figure 5. Structures of opposite sign tend to be associated with the periphery of the core of the AR.

3.6. Isotropy Assumption for Magnetic Helicity Spectra

As discussed above, under the assumption of isotropy, the magnetic and current helicity spectra are related to each other through Equation (13). It was already clear from Figure 5 that this assumption holds reasonably well. The purpose of this section is to analyze this in more detail. Therefore, we show in Figure 8 scatter plots of $\mu_0 H_C(k)$ versus $k^2 H_M(k)$ for the same six heights as in Figure 5. It turns out that most of the data points lie on the diagonal, which covers about eight orders of magnitude. Some of the data points, however, have mutually opposite signs, which correspond to an anticorrelation. Thus, Equation (13) holds primarily for the moduli of $H_C(k)$ and $H_M(k)$.

The fact that some of the data points have the opposite sign was already evident when examining the colors in Figure 5. Below $z = 5 \text{ Mm}$, about 80% of the points have the expected sign, but at higher levels, the number of exceptions increases. For large values of $|H_M(k)|$, and especially for $z > 5 \text{ Mm}$, there is a noticeable number of data points below the diagonal, i.e., $|H_C(k)|$ is somewhat smaller than expected.

It is clear from Figure 5 that $H_M(k)$ shows fewer sign reversals with k than $H_C(k)$ and shows a more systematic behavior in that sense. One would therefore be tempted to trust the magnetic helicity spectra more than the current helicity spectra. However, two other considerations come to mind.

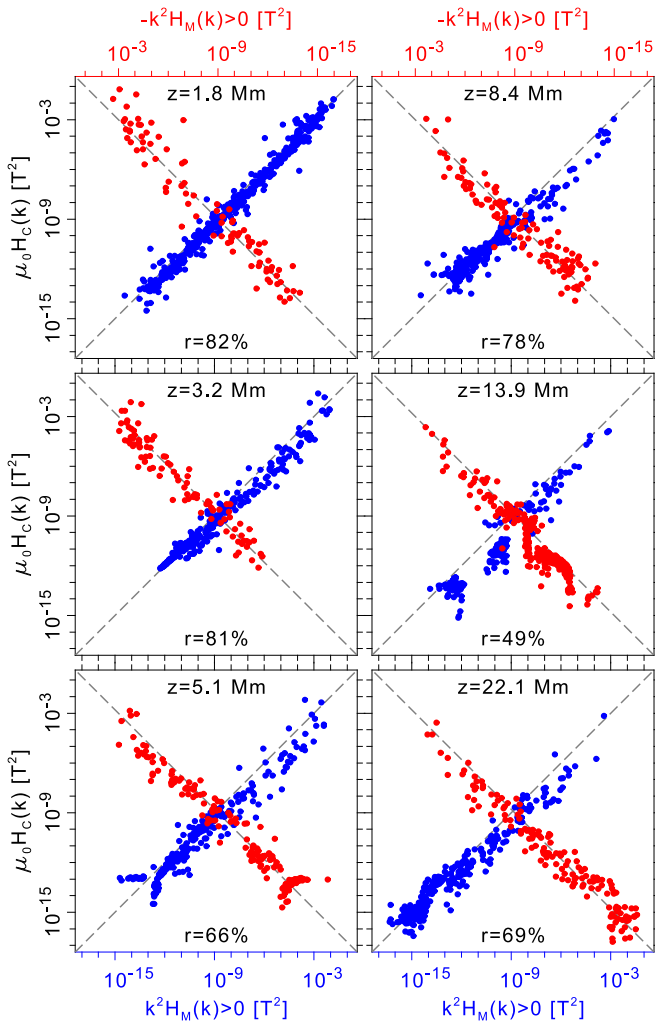


Figure 8. Correlation (blue) and anticorrelation (red) in the magnetic and current helicity. The sampling height z and the percentage of correlated points r are given in each panel.

First, both spectra are intrinsically noisy and one can expect meaningful results only after some degree of averaging. This could be accomplished by averaging the spectra over broader wavenumber bins. Second, Equation (13) is only valid under the assumption of isotropy. Again, this statement only applies in the statistical sense, i.e., after sufficient averaging. This is particularly evident in the present case where there is only one AR with its resulting coronal structure. In view of these caveats, one must say that the agreement found in Figure 8 is actually rather remarkable.

4. Conclusions

The present work has elucidated the phenomenon of a magnetic helicity reversal above a magnetized layer in general and along a coronal loop in particular. We have seen that this reversal is the result of a change in the relative dominance of structures of opposite magnetic helicity. As a consequence, in a particular simulation, this change in sign happens abruptly. It also happens at all wavenumbers at the same height. Of course, given that this change of sign depends on the subtle dominance of structures of one sign over the other, we should expect that in other simulations or at other times in the same simulation,

such a reversal can occur at different heights. However, we also have found that the magnetic helicity reversal happens near the location where the plasma beta changes from values above unity to values below unity, i.e., when the field becomes almost force free; see the horizontal gray dashed line in Figure 2, as well as the crossing red and black lines in Figure 3. This gives us for the first time a fairly strong handle on this remarkable phenomenon of a magnetic helicity reversal above a dynamo-active region.

It is important to note that the helicity in the lower atmosphere of our simulations has the sign expected for the southern hemisphere, even though there is neither a direct injection of helicity nor a mechanism to break the north–south symmetry in the model, except for the imposed photospheric magnetogram. A possible explanation is that the dynamo and the differential rotation inside the Sun leave imprints in the photospheric magnetic fields. These should then be sufficient to infer the signs of the average helicities in the lower and upper corona. As shown in Bourdin & Brandenburg (2018), any arrangement of more than two spots of unequal strength implies a non-mirrorsymmetric pattern, which can give rise to a certain sign of magnetic helicity in the force-free magnetic field above the surface.

Thinking now about the Sun and the solar wind, we expect the magnetic helicity reversal to occur well within the solar corona and not between the corona and the location of the Earth. Thus, we expect that the magnetometers on the *Parker Solar Probe* and *SolarOrbiter* will measure the same sign of magnetic helicity as what is observed in Earth’s neighborhood, which is opposite to what is found at the solar surface. The sign of course should flip if one of the measurement points is magnetically connected to the other magnetic hemisphere of the Sun, which typically happens if one crosses the heliospheric current sheet (HCS). This becomes more likely during high solar activity because then the HCS may strongly deviate from the ecliptic plane. Perhaps the only feasible way to verify a magnetic helicity reversal so close to the surface is by determining the wavelength at which Faraday depolarization from intrinsic coronal emission is minimized (Brandenburg et al. 2017). This would require observations at infrared and millimeter wavelengths just above the limb.

This work is financially supported by the Austrian Space Applications Programme at the Austrian Research Promotion Agency, FFG ASAP-12 SOPHIE under contract 853994. The results of this research have been achieved using the PRACE Research Infrastructure resource *Curie* based in France at TGCC, as well as *JuRoPA* hosted by the Jülich Supercomputing Centre in Germany. Hinode is a Japanese mission developed, launched, and operated by ISAS/JAXA, in partnership with NAOJ, NASA, and STFC (UK). Additional operational support is provided by ESA and NSC (Norway). This research was supported in part by the NSF Astronomy and Astrophysics Grants Program (grant 1615100), and the University of Colorado through its support of the George Ellery Hale visiting faculty appointment.

ORCID iDs

Philippe Bourdin <https://orcid.org/0000-0002-6793-601X>
 Nishant K. Singh <https://orcid.org/0000-0001-6097-688X>
 Axel Brandenburg <https://orcid.org/0000-0002-7304-021X>

References

- Berger, M. A., & Field, G. B. 1984, *JFM*, **147**, 133
- Berger, M. A., & Ruzmaikin, A. 2000, *JGR*, **105**, 10481
- Biskamp, D. 2003, *Magnetohydrodynamic Turbulence* (Cambridge: Cambridge Univ. Press)
- Blackman, E. G., & Brandenburg, A. 2003, *ApJL*, **584**, L99
- Blackman, E. G., & Field, G. B. 2000, *MNRAS*, **318**, 724
- Bonanno, A. 2016, *ApJL*, **833**, L22
- Bourdin, P.-A. 2014, *CEAB*, **38**, 1
- Bourdin, P.-A. 2017, *ApJL*, **850**, L29
- Bourdin, P.-A., Bingert, S., & Peter, H. 2013, *A&A*, **555**, A123, (BBP)
- Bourdin, P.-A., Bingert, S., & Peter, H. 2014, *PASJ*, **66**, S78
- Bourdin, P.-A., Bingert, S., & Peter, H. 2015, *A&A*, **580**, A72
- Bourdin, P.-A., Bingert, S., & Peter, H. 2016, *A&A*, **589**, A86
- Bourdin, P.-A., & Brandenburg, A. 2018, *ApJ*, **869**, 3
- Brandenburg, A. 2009, *PPCF*, **51**, 124043
- Brandenburg, A. 2014, *ApJ*, **791**, 12
- Brandenburg, A., Ashurova, M. B., & Jabbari, S. 2017, *ApJL*, **845**, L15
- Brandenburg, A., Candelaresi, S., & Chatterjee, P. 2009, *MNRAS*, **398**, 1414
- Brandenburg, A., & Sandin, C. 2004, *A&A*, **427**, 13
- Brandenburg, A., & Subramanian, K. 2005, *PhR*, **417**, 1
- Brandenburg, A., Subramanian, K., Balogh, A., & Goldstein, M. L. 2011, *ApJ*, **734**, 9
- Christensson, M., Hindmarsh, M., & Brandenburg, A. 2001, *PhRvE*, **64**, 056405
- Cook, J. W., Cheng, C.-C., Jacobs, V. L., & Antiochos, S. K. 1989, *ApJ*, **338**, 1176
- Culhane, J. L., Harra, L. K., James, A. M., et al. 2007, *SoPh*, **243**, 19
- Dere, K. P., Landi, E., Mason, H. E., Monsignori Fossi, B. C., & Young, P. R. 1997, *A&AS*, **125**, 149
- DeVore, C. R. 2000, *ApJ*, **539**, 944
- Finn, J. M., & Antonsen, T. M., Jr. 1985, *Comments Plasma Phys. Controlled Fusion*, **9**, 111
- Gruzinov, A. V., & Diamond, P. H. 1994, *PhRvL*, **72**, 1651
- Gudiksen, B., & Nordlund, Å. 2002, *ApJL*, **572**, L113
- Gudiksen, B., & Nordlund, Å. 2005a, *ApJ*, **618**, 1020
- Gudiksen, B., & Nordlund, Å. 2005b, *ApJ*, **618**, 1031
- Ji, H. 1999, *PhRvL*, **83**, 3198
- Kleeorin, N., Moss, D., Rogachevskii, I., & Sokoloff, D. 2000, *A&A*, **361**, L5
- Kosugi, T., Matsuzaki, K., Sakao, T., et al. 2007, *SoPh*, **243**, 3
- Krause, F., & Rädler, K.-H. 1980, *Mean-field Magnetohydrodynamics and Dynamo Theory* (Oxford: Pergamon)
- Moffatt, H. K. 1978, *Magnetic Field Generation in Electrically Conducting Fluids* (Cambridge: Cambridge Univ. Press)
- Parker, E. N. 1972, *ApJ*, **174**, 499
- Peter, H., Gudiksen, B., & Nordlund, Å. 2004, *ApJL*, **617**, L85
- Peter, H., Gudiksen, B., & Nordlund, Å. 2006, *ApJ*, **638**, 1086
- Rempel, M. 2017, *ApJ*, **834**, 10
- Seehafer, N. 1990, *SoPh*, **125**, 219
- Seehafer, N. 1996, *PhRvE*, **53**, 1283
- Tsuneta, S., Ichimoto, K., Katsukawa, Y., et al. 2008, *SoPh*, **249**, 167
- Warnecke, J., & Brandenburg, A. 2010, *A&A*, **523**, A19
- Warnecke, J., Brandenburg, A., & Mitra, D. 2011, *A&A*, **534**, A11
- Warnecke, J., Brandenburg, A., & Mitra, D. 2012, *JSWSC*, **2**, A11
- Woltjer, L. 1958, *PNAS*, **44**, 489
- Young, P. R., Del Zanna, G., Landi, E., et al. 2003, *ApJS*, **144**, 135
- Yousef, T. A., & Brandenburg, A. 2003, *A&A*, **407**, 7